Chapter 4

Empirical Demonstration and Investigation of Propulsive Performance

4.1 Introduction

This chapter describes the characterization of the jet flow and the investigation of the propulsive performance of the vehicle. Section 4.2 describes the experimental procedures and conditions that existed during experimentation. In section 4.3, the jet is characterized using two different experimental techniques, digital particle image velocimetry and planar laser-induced fluorescence. More specifically, section 4.3.1 shows the results obtained from the digital particle image velocimetry experiments. This technique was used to select an inner shell geometry for the pulsed jet configuration and to make comparisons between the steady and unsteady jet flow field. In section 4.3.2, the results obtained from the planar laser-induced fluorescence experiments were used as a tool for flow visualization. They provide insight on the behavior of the jet flow for both the steady and pulsed jet mode of propulsion. Section 4.4 shows results of propulsive performance measurements for three modes of vehicle propulsion. The configurations consisted of the steady jet with the inner rotating shell, the steady jet without the inner rotating shell and the pulsed jet. Initially the Froude efficiency of the vehicle was used as a propulsive performance metric. The results are displayed in section 4.4.1. It was discovered that increased Froude efficiencies may exist at higher vehicle speeds. This concept is explored in section 4.4.2. Another metric, the total hydrodynamic efficiency, was used to make

comparisons of the propulsive performance between the different modes of propulsion. The results from these experiments are found in section 4.4.3. Section 4.5 examines the propulsive efficiency observed in biological organisms. Finally, section 4.6 discusses the power coefficient and how it was measured to determine if a trade-off existed between improved propulsive performance and power consumption.

4.2 Experimental Conditions

The vehicle was held in a stationary position for the jet characterization results in section 4.3. The vehicle was set to operate at a constant motor speed. As a simplification, no inner rotating shell was used for the duration of the experiments in the steady propulsion mode. The rotational speed of the propeller was between 480 and 500 rpm. For the unsteady jet experiments, the geometry of the inner rotating shell was varied to observe the effects on jet dynamics. The rotational speed of the propeller was in the range of 650 to 730 rpm. Two fluid vents located on the top side of the vehicle were blocked using electrical tape upon discovering that it was necessary to decrease the pulsing frequency. Only the bottom fluid vent remained open. Given that the rotational rate of the inner shell is geared down by a ratio of 5 from the rotational rate of the propeller, the pulsing frequency ranged from 2.2 to 2.5 Hz. Both DPIV and PLIF measurements were made in spans ranging between 5 and 10 seconds. Numerous runs were conducted for each motor speed to ensure repeatability and reduce measurement noise.

To evaluate the propulsive performance of the steady and pulsed jet mode of propulsion, it was necessary to conduct these experiments during self-propulsion. The vehicle was set to propel down the facility at approximately the same start position. While in motion, the power consumed by the system, the rotational speed on the motor shaft, and the jet velocity were measured. The velocity of the vehicle was measured indirectly by recording the velocity of the motorized traverse that tracked the vehicle at a preset distance of 40 cm. Depending on the speed of the vehicle, 5 to 10 seconds of data was acquired per run. Sufficient time was necessary to allow for temporal averaging to reduce measurement noise. Only the axial jet velocity at the center of the jet was measured using LDV

given that the axial jet velocity along the radial direction of the jet is constant. See section 5.4.1.

Initial propulsive performance studies were conducted for three vehicle configurations, the steady jet with the inner rotating shell, the steady jet without the inner rotating shell and the pulsed jet. It was discovered from the characterization studies that an inner shell opening of 300^o was necessary to produce a pulsed jet with vortex ring formation. Fifteen trials of experiments were conducted with this inner shell geometry. The rotational speed of the propeller ranged from 2540 to 2960 rpm. A total of 16 trials were performed with an inner shell geometry producing a steady jet with an equivalent mechanical efficiency as the unsteady configuration. The rotational rate of the propeller operated in a range of 2580 to 2920 rpm. Finally, 16 baseline trials were performed in a steady configuration without an inner rotational shell. The propeller rotational rate for these cases ranged from 2420 to 2970 rpm. Difficulties arose in reaching and maintaining higher rotation speeds than those tested due to input power requirements.

Another series of performance studies was conducted to observe the propulsive performance at higher vehicle speeds. A 60 V power supply was used to supply the constant power necessary for the vehicle to attain higher speeds. The original motor was replaced due to mechanical failure. The performance of the new motor varied from the original despite using the same model. It was observed that an increased propeller rotational speed was necessary to achieve the same vehicle speed, therefore decreasing the pulse duration.

Two sets of experiments were conducted for the secondary study. A total of 12 experiments were conducted evaluating the propulsive performance of the unsteady mode of propulsion. The rotational rate of the propeller varied from 2740 to 3770 rpm. Twelve experiments of the steady jet configuration without the rotational shell were performed as comparison. The steady shell was not used in order to simplify the experiments and to decrease motor stress. The rotation rate of the propeller spanned 2900 to 3830 rpm. The power supplied directly to the motor was measured and recorded in addition to system power usage.

4.3 Jet Characterization: Flow Visualization

4.3.1 PIV Measurements

4.3.1.1 Inner Shell Modification and Effect to Unsteady Jet Formation

The initial inner shell geometry was designed with three 26^o fluid openings. See figure 4.1(a) where θ_{io} is the inner rotational fluid shell opening. One complete revolution of the inner shell results in 3 instances in time where the fluid vents were aligned, resulting in 3 jet pulses per revolution. An instance of the velocity field of the jet obtained using DPIV is shown in figure 4.2. The motor was operating at 671 rpm during this particular trial, hence, the fluid vents aligned at a frequency of 7.70 Hz. The Reynolds number, Re_j of the jet based on the average jet velocity, U_{avg}, and D, the exit jet diameter, was 2700.

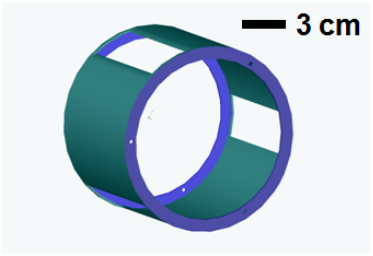

(a) Shell with $\theta_{io} = 26^o$ and $t^* \approx 0.038$.

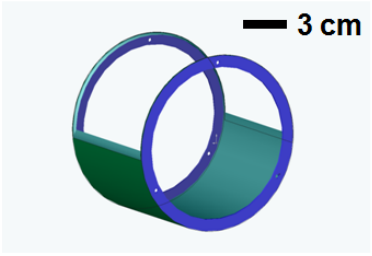

(b) Shell with $\theta_{io} = 180^o$ and $t^* \approx 0.321$.

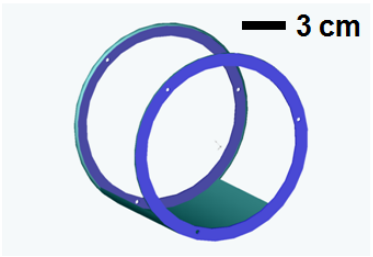

(c) Shell with $\theta_{io} = 270^o$ and $t^* \approx 0.472$.

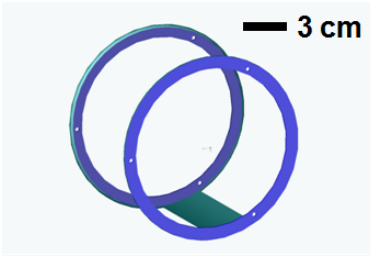

(d) Shell with $\theta_{io} = 334^o$ and $t^* \approx 0.888$.

Figure 4.1. Inner shell geometries tested. The shell with $\theta_{io} = 334^o$ was selected for the propulsive performance studies.

The formation time, t^*, was also measured and used to characterize the jet flow. The formation time is the nondimensional time equivalent to the ratio of the length to the diameter of an ejected fluid column otherwise known as the stroke ratio (Gharib et al. 1998). It is expressed as

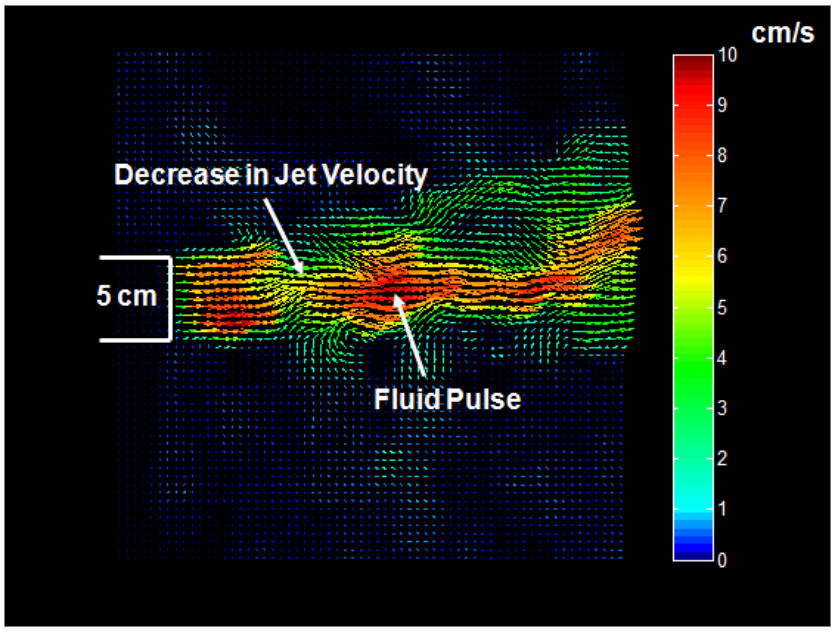

Figure 4.2. Instantaneous velocity field of the jet with the vehicle configured with the 26^o fluid opening for the inner shell geometry.

$$t^* = \frac{U_{avg}\, t}{D}, \tag{4.1}$$

where $t = \theta_{io}/\,\omega$ is the fluid discharge time or the amount of time the fluid vents are aligned per pulse duration and ω is the angular velocity of the inner rotating shell.

From figure 4.2 it is evident that no vortex ring formation is present with this shell geometry. Pulsing of the jet is evident by a period of time where the core jet velocity is 10 cm/s followed by a period of time where the jet velocity decreases to 5 cm/s. Using the measurement of U_{avg} obtained from the DPIV data, the formation time was calculated to be 0.04 for the case of the vehicle configured with the 26^o degree fluid opening in the inner shell geometry operating at a motor speed of 670 rpm.

Didden (1979) noted that isolated vortex rings could not be produced for $t^* < 0.4$. Given this condition on t^*, θ_{io} was increased in an effort to increase the fluid discharge time. As a consequence of increasing θ_{io}, the two fluid vents located on the top of the submarine were blocked with electrical tape to prevent the inner shell opening from overlapping with more than one fluid vent at a time.

The inner shell was redesigned allowing for only one fluid opening per revolution of the shell.

DPIV experiments were then conducted on the vehicle jet with the motor operating at 640 rpm and a 180^o fluid opening for the inner shell geometry. See figure 4.1(b) for the geometry of the shell. The pulsing frequency was 2.15 Hz as the inner fluid vent aligned with the outer fluid once per revolution. Re_j was 3175 and t^* reached a value of 0.32. The velocity in the core center of each pulse reached a velocity of 14 cm/s. In contrast to the previous experiments conducted with the 26^o inner fluid opening, it was now apparent that ambient flow near the jet exit was entrained into the jet during the formation of a pulse. These flow characteristics can be seen in figure 4.3(a).

The inner fluid shell opening was further increased to 270^o. See figure 4.1(c) for the geometry of the shell. DPIV experiments were conducted on the jet flow of the vehicle with the motor operating at a comparable rotational speed to previous experiments. The rotational speed was 650 rpm giving a pulsing frequency of 2.2 Hz. This increase in shell opening led to a further increase in t^* to a value of 0.47. The Re_j for the jet flow was 3630. With the increased inner shell fluid opening, the velocity in the core of the pulse had a corresponding increase to 20 cm/s. Flow roll up was now apparent which is suggestive of vortex ring formation. See figure 4.3(b).

To further increase the fluid roll up, t^* was increased by increasing the size of the inner shell fluid opening to 334^o. The geometry of this inner rotational shell can be seen in figure 4.1(d). The motor was set to operate at 740 rpm producing a pulsing frequency of 2.5 Hz. At this rotation speed, Re_j was equal to 5443 and t^* increased to 0.89. Vortex ring formation was apparent with this inner shell geometry. See figure 4.4(a). The maximum velocity in core of the vortex reached 35 cm/s. The vorticity contour is also illustrated for this instantaneous velocity field in figure 4.4(b). The vorticity contour demonstrates symmetric vorticity along the jet centerline. This shell geometry with $\theta_{io} = 334^o$ was used for the remainder of the propulsive performance studies.

4.3.1.2 Steady Jet Configuration

DPIV experiments were also performed on the vehicle for the steady mode of propulsion without the inner rotating shell. The velocity field demonstrates a uniform field with the jet achieving a

maximum velocity of 25 cm/s and a Re_j of 7250. See figure 4.5. The jet maintains a cylindrical shape until 1.5 jet diameters downstream. Downstream from this point, instabilities in the shear layer break up the cylindrical shape of the jet, and the jet appears less ordered and no longer round. There is significantly less entrainment near the nozzle exit in comparison to the unsteady mode of propulsion with the inner shell geometry of $\theta_{io} = 334^o$.

4.3.2 PLIF Measurements

PLIF experiments were conducted for both the steady mode of propulsion without the inner rotating shell and the unsteady mode of propulsion with the inner shell geometry of $\theta_{io} = 334^o$. For these experiments, the rotational speed of the motor for the steady configuration was 500 rpm and 730 rpm for the unsteady configuration. For the pulsed jet configuration, entrainment of the ambient flow into the vortex ring is illustrated by the dark regions within the vortex ring in figure 4.6. The additional mass transfer into the vortex led to a larger wake size in comparison to the the steady jet as a result of vortex ring formation.

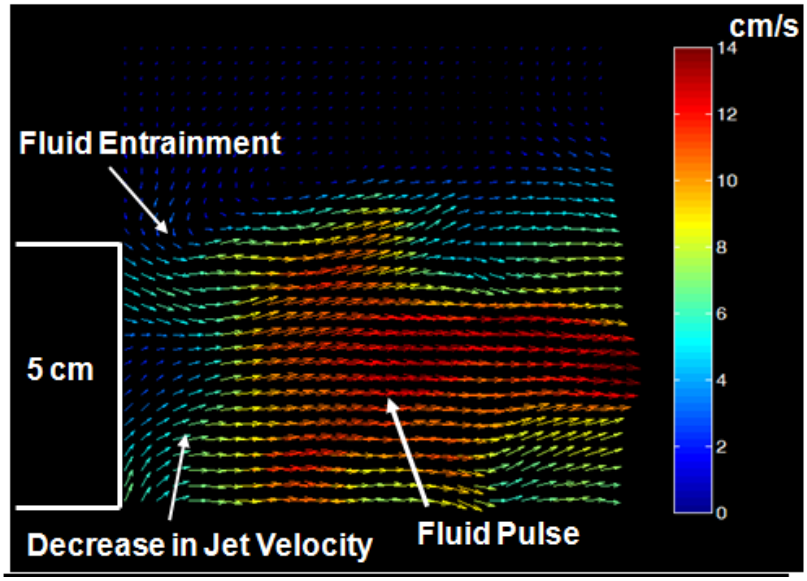

(a) Vehicle configured with the 180^o fluid opening inner shell geometry.

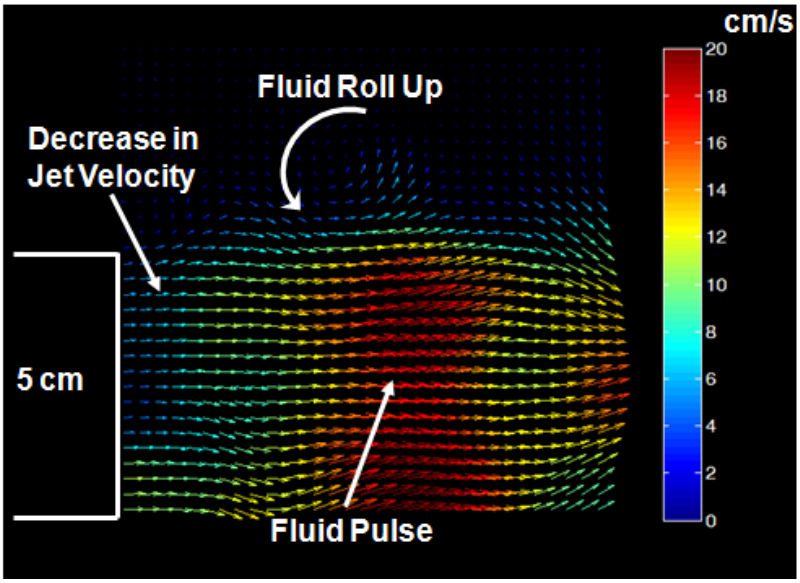

(b) Vehicle configured with the 270^o fluid opening inner shell geometry.

Figure 4.3. Instantaneous velocity field of the jet with the vehicle configured with two unsteady shell geometries.

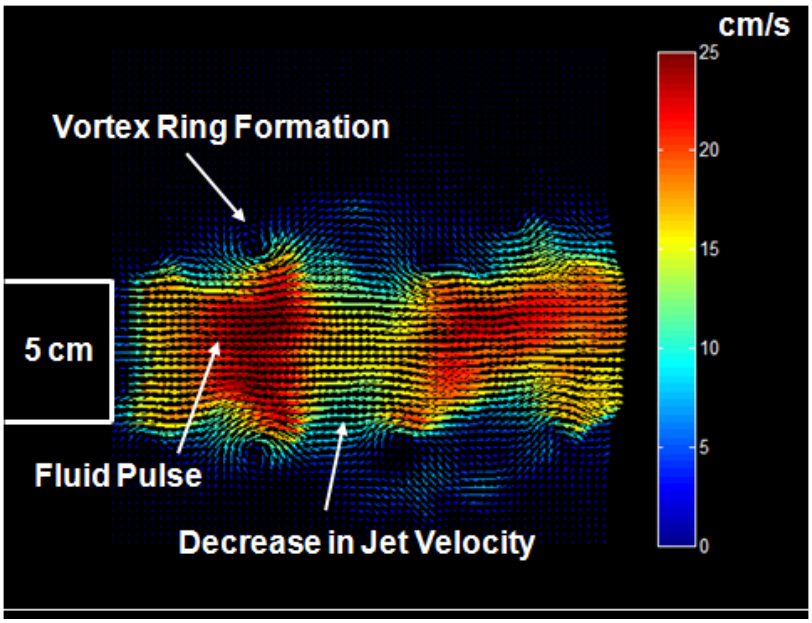

(a) Instantaneous Velocity field illustrating vortex ring formation.

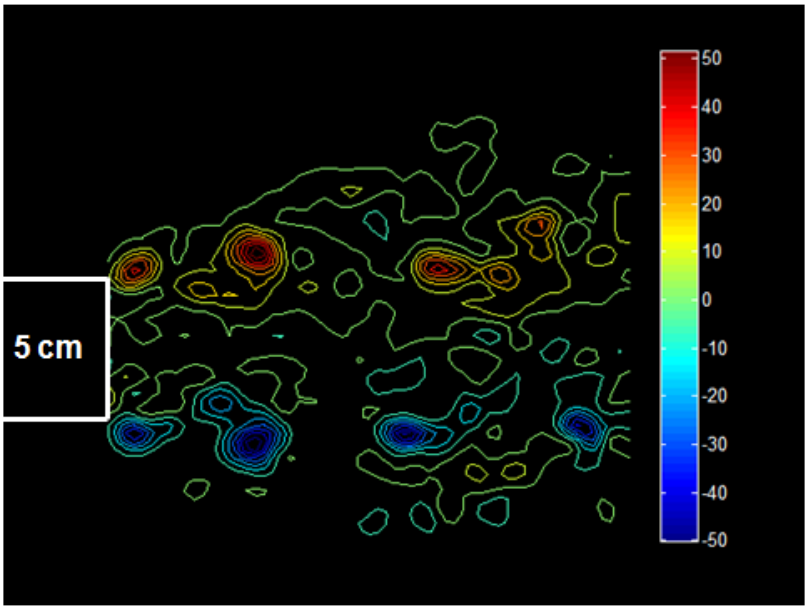

(b) Vorticity contour illustrating symmetric vorticity along jet centerline.

Figure 4.4. Instantaneous velocity field and vorticity contour of the jet with vehicle configured using final unsteady shell geometry with $\theta_{io} = 334^o$.

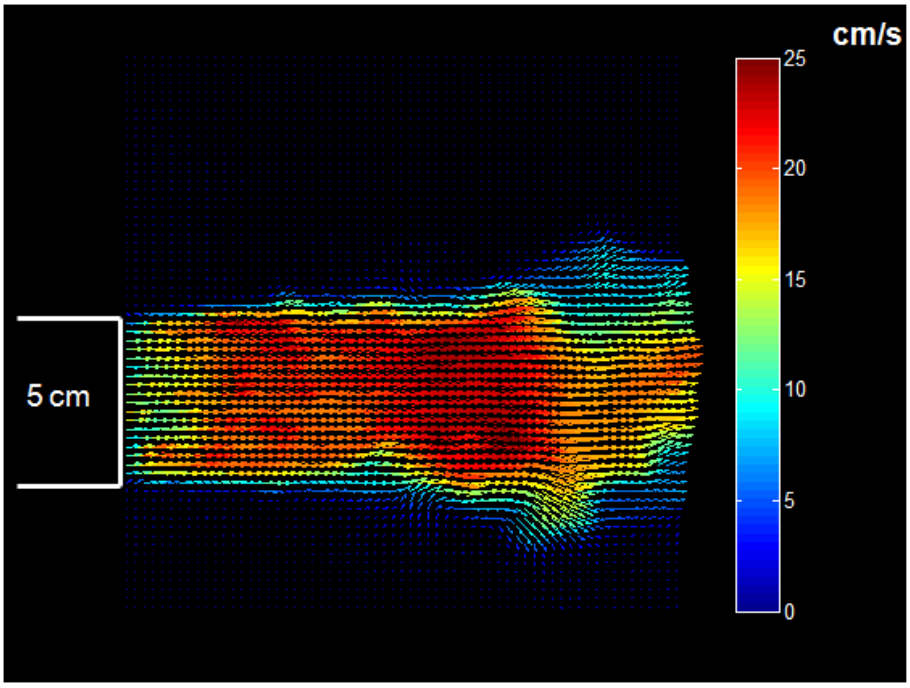

Figure 4.5. Instantaneous velocity field of the jet with vehicle in steady mode of propulsion without the inner rotational shell.

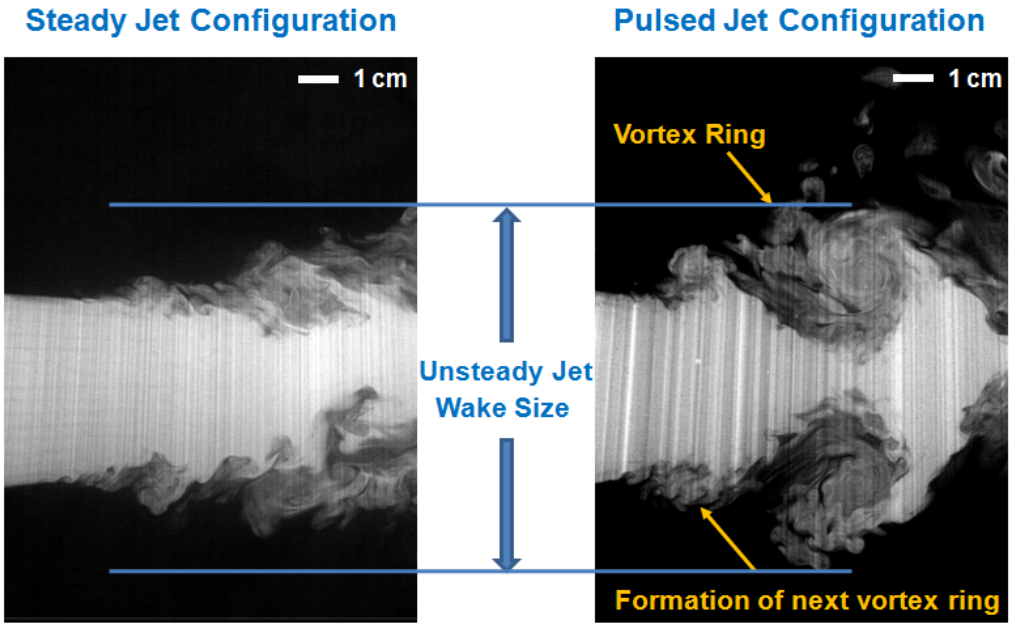

Figure 4.6. PLIF images illustrating a larger wake size for the pulsed jet in comparison to the steady jet due to the formation of vortex rings.

4.4 Measurement of Propulsive Performance

The data obtained from both propulsive performance studies is cataloged in Appendix E. Included with the data are the standard deviations in the measurements. The average standard deviation in the motor speed was 30 rpm. The average standard deviation in the vehicle speed was 3.2 cm/s for the first set of propulsive performance studies. The standard deviation in vehicle speed increased to 5 cm/s for the second set of data obtained using the second motor. It is important to note that although the jet efflux is unsteady for the pulsed jet configuration, the mass of the vehicle acts as a low-pass filter such that oscillations in the cruising velocity are negligible. The deviation in mean speed is due to the nonuniform drag force experienced by the vehicle as it translates along the flume facility and the ability of the speed controller to maintain a constant motor speed. Figure 4.7 illustrates the variation in the speed of the vehicle over the duration of the experiment for both the pulsed jet and steady jet without the rotating shell. It is apparent from the figure that the variation in vehicle speed for the pulsed jet configuration does not coincide with the pulsing frequency.

4.4.1 Comparison of Froude Efficiency for Both Steady and Unsteady Jet Propulsion

For the first set of propulsive performance studies the Froude efficiency was measured for three vehicle configurations, the steady jet with the inner rotating shell, the steady jet without the inner rotating shell and the pulsed jet. The Froude efficiency was calculated using equation (4.2),

$$\eta_F = \frac{2}{1 + U_{avg}/U_v}, \tag{4.2}$$

where U_{avg} is the average jet velocity and U_v is the average vehicle speed. Given that the Froude efficiency applies for a body moving at steady state velocity, the standard deviation in U_v was used to compute the error in the measurement of the efficiency.

Figure 4.8 is a plot of the Froude efficiency versus motor speed for the three modes of propulsion. At the lower motor speeds tested, it is difficult to determine whether a potential benefit exists with

pulsed jet propulsion given the uncertainty in the measurement. As the motor speed increases, the Froude efficiency for the pulsed jet increases at a higher rate in comparison to both steady types. In order to gain an understanding of the magnitude of the increased Froude efficiency generated by using a pulsed jet for propulsion, the data was normalized by the baseline case of the steady jet without the rotating shell. See figure 4.9. The steady jet without the rotating shell is denoted as SWOS. A value of 1 for all motor speeds denotes the normalized efficiency for the steady jet without the rotating shell, and the gray band signifies the uncertainty in the measurement. The Froude efficiency increased linearly with motor speed for all modes of propulsion. The pulsed jet has a higher Froude efficiency in comparison to both steady types for most motor speeds. On average, the pulsed jet has a 40% increase in the Froude efficiency at higher motor speeds. The steady jet with the rotating shell falls within the uncertainty of the steady jet without the rotating shell for most values of normalized efficiency.

The Froude efficiency was also measured for the data obtained using the second motor. The results are shown in figure 4.10. The goal of this set of experiments was to observe the change in Froude efficiency at higher motor speeds. Similar trends were observed with this set of data in comparison to the first data series. The Froude efficiency increased linearly with motor speeds for both modes of propulsion. At the lower motor speeds tested, it is difficult to determine whether a potential benefit exists with pulsed jet propulsion given the uncertainty in the measurement. Similar to previous experiments, as the motor speed increases, the Froude efficiency increases at a higher rate for the pulsed jet mode of propulsion in comparison to the steady jet. The Froude efficiency was normalized by the Froude efficiency of the steady jet without the rotating shell, as shown in figure 4.11. At the higher motor speeds, the pulsed jet achieved on average a 20% increase in Froude efficiency in comparison to the steady jet without the rotating shell. This increase in Froude efficiency is 50% lower than observed with the first series of experiments. To gain an understanding of the source of the difference, the Froude efficiency for all the experiments were plotted together versus motor speed. See figure 4.12.

It is apparent that similar trends exist between both data sets from the compiled Froude efficiency

measurements, however, the results are shifted in motor speed. Another difference is evident in the rate of increase in the measure of Froude efficiency for the pulsed jet mode of propulsion. The rate of increase is steeper for the initial motor results. For the second motor, the motor speed was increased in order to produce an equivalent average jet speed generated using the initial motor. See figure 4.13. The formation time for vortex ring formation was calculated using equation (4.1). The formation time had a corresponding decrease as a result of the increase in motor speed, as shown in figure 4.14. The formation time was greater using the initial motor for a given vehicle speed with the exception of one point. This leads to a larger formation time and an increased impulse generated by the developing vortex ring (Krueger and Gharib 2003). This explains the increase in propulsive performance.

4.4.2 Effects of Increased Vehicle Speed on Froude Efficiency Model

The relationship between jet velocity and vehicle speed was examined to determine the effect of increased vehicle speed on Froude efficiency. Figure 4.15 is a plot of the average temporal jet velocity, U_{avg}, versus the average vehicle speed, U_v, for experiments conducted with the initial motor. The average jet velocity approaches a steady state velocity of 160 cm/s as motor speed increases. The following dashed curve is generated as shown in figure 4.16 by taking the average jet velocity of 160 cm/s and plugging it into the Froude efficiency.

The data obtained using the initial motor was included and plotted in the figure. The data resides on the bottom portion of the dashed curve of the Froude efficiency model. Although the maximum motor speed was comparable among all modes of propulsion, the highest measurement in the Froude efficiency was obtained for the experiments using pulsed jet propulsion. Initial propulsive performance studies suggested that there may be further increases in the Froude efficiency at higher motor speeds. To investigate this possibility, experiments were conducted at higher motor speeds with the secondary motor. A few experiments were conducted at comparable motor speeds to the first series of experiments to verify repeatability. The results from the higher speed experiments were plotted against the model of the Froude efficiency with an average jet velocity of 180 cm/s in

figure 4.17. The higher speed results continue to follow the modeled dashed curve. With increased vehicle speed, the Froude efficiency reached a maximum value of 47% for the pulsed jet configuration. Whether the Froude efficiency would continue to increase could not be determined from the data. It is important to note that as the body velocity approaches the jet velocity, the thrust approaches zero since the thrust is approximated as $\dot{m}(U_{avg} - U_v)$ in the derivation of the Froude efficiency.

4.4.3 Comparison of Total Hydrodynamic Efficiency for Both Steady and Unsteady Jet Propulsion

Another metric for the measure of propulsive performance is the total hydrodynamic efficiency. The total hydrodynamic efficiency is defined as the ratio of useful work over the useful work plus wasted energy. The useful work is the product of the thrust and the vehicle speed. The wasted energy is defined as any kinetic energy left in the wake as a result of jetting relative to the surrounding flow and is equal to the product of $\frac{1}{2}\rho\, A_j\, U_{avg}\,(U_{avg} - U_v)^2$. Making the substitution for useful work and wasted energy into the definition of the total hydrodynamic efficiency, the following result is obtained,

$$\eta_{hydro} = \frac{useful\ work}{useful\ work\ +\ wasted\ energy} = \frac{D\,U_v}{D\,U_v\ +\ \frac{1}{2}\rho\, A_j\, U_{avg}\,(U_{avg} - U_v)^2}, \tag{4.3}$$

where A_j is the area of the jet exit. Given that the system is traveling at steady state, the thrust produced by the system is equivalent to the drag. The drag was measured in an independent experiment, as described in section 3.4.5. The definition of the total hydrodynamic efficiency does not make any approximation of the drag in contrast to the Froude efficiency.

For the first set of propulsive performance studies, the total hydrodynamic efficiency was measured for three vehicle configurations, the steady jet with the inner rotating shell, the steady jet without the inner rotating shell and the pulsed jet. Given that the vehicle is assumed to be traveling at steady state, the standard deviation in the vehicle speed was used to generate the error in the measurement of the efficiency. Figure 4.18 shows the relationship between the total hydrodynamic

efficiency versus motor speed. Similar to the results of the propulsive efficiency, at lower motor speeds, it is difficult to infer whether the pulsed jet produces an increase in efficiency over both steady jet types within the uncertainty of the measurement. At higher motor speeds it is evident that the pulsed jet is superior to both steady jet types. The pulsed jet acquired maximum total hydrodynamic efficiency of 54% at a motor speed of 2890 rpm. The normalized total hydrodynamic efficiency versus motor speed is shown in figure 4.19. At motor speeds above 2800 rpm, there is a 57% average increase in the total hydrodynamic efficiency of the pulsed jet in comparison to the steady jet. With the exception of a few data points, the results for the steady jet with the rotating shell fall within the measurement uncertainty of the normalized hydrodynamic efficiency for the steady jet without the rotating shell.

The results of total hydrodynamic efficiency versus motor speed for the second motor are shown in figure 4.20. It is apparent that the pulsed jet produces a higher total hydrodynamic efficiency at motor speeds higher than 3500 rpm. The total hydrodynamic efficiency reached the highest value of 63% at a motor speed of 3770 rpm for the vehicle traveling in the pulsed jet configuration. There is an average 32% increase in the hydrodynamic efficiency for the pulsed jet at motor speeds above 3500 rpm after normalizing the hydrodynamic efficiency by the results for the steady jet without the rotating shell.

Measurements of the total hydrodynamic efficiency for both series of experiments can be analyzed in figure 4.22. The results from the second study of hydrodynamic efficiency are shifted in motor speed similarly to the compiled results of the propulsive efficiency. The rate of increase in the hydrodynamic efficiency for the initial pulsed jet experiments is greater in comparison to the measurements obtained with the second motor. The decrease in performance for the second motor can be attributed to a decrease in the vortex ring formation time.

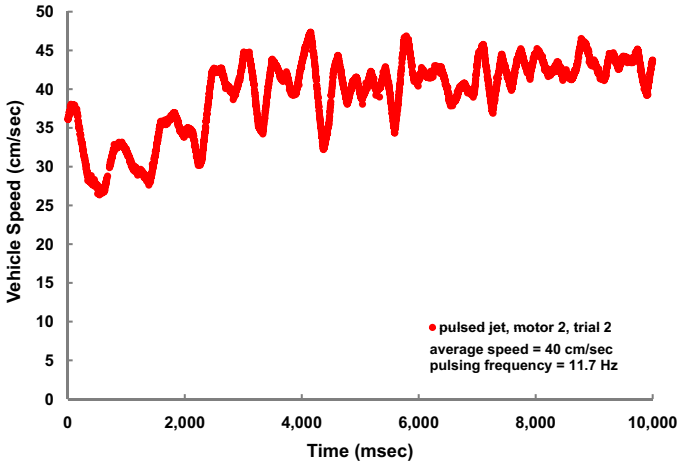

(a) Vehicle speed obtained using a pulsed jet.

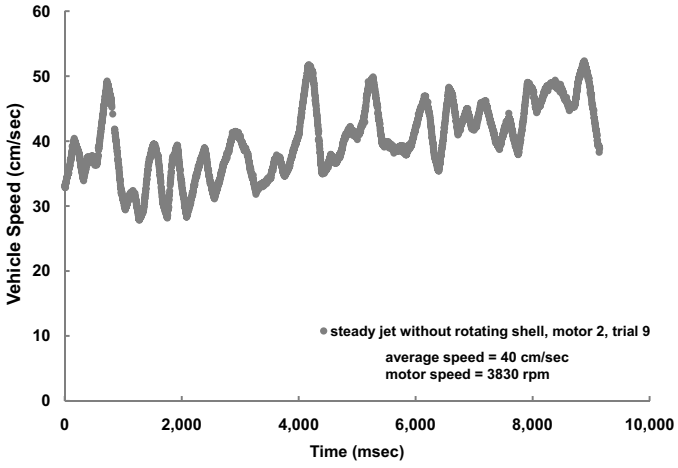

(b) Vehicle speed obtained using a steady jet without the inner rotating shell.

Figure 4.7. Illustration of typical variation in vehicle speed over the duration of an experiment.

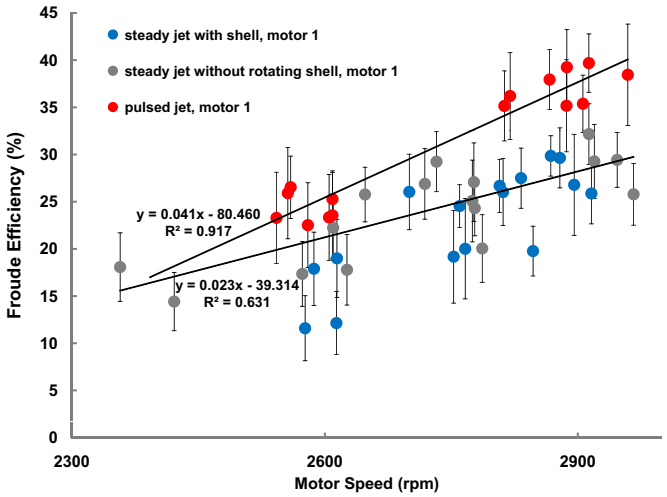

Figure 4.8. Froude efficiency versus motor speed for motor 1.

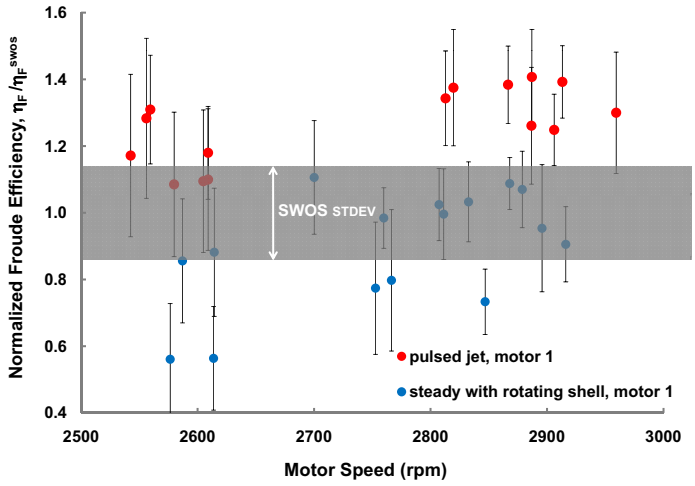

Figure 4.9. Normalized Froude efficiency versus motor speed for motor 1.

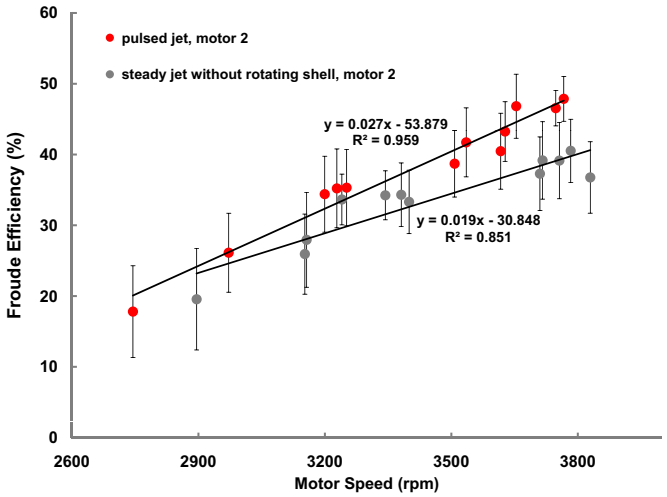

Figure 4.10. Froude efficiency versus motor speed for motor 2.

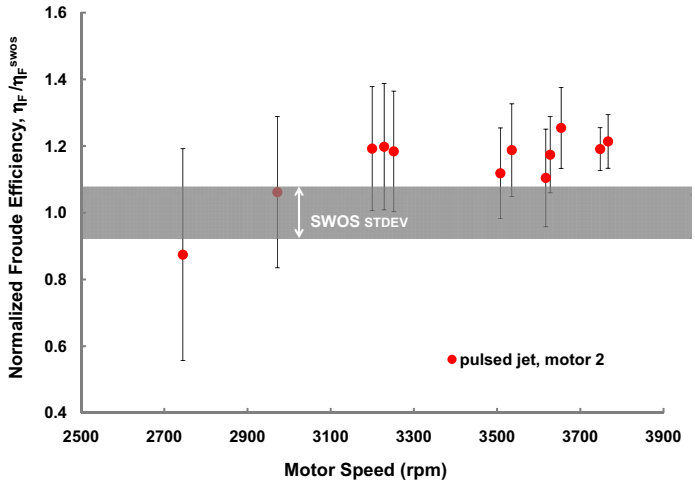

Figure 4.11. Normalized Froude efficiency versus motor speed for motor 2.

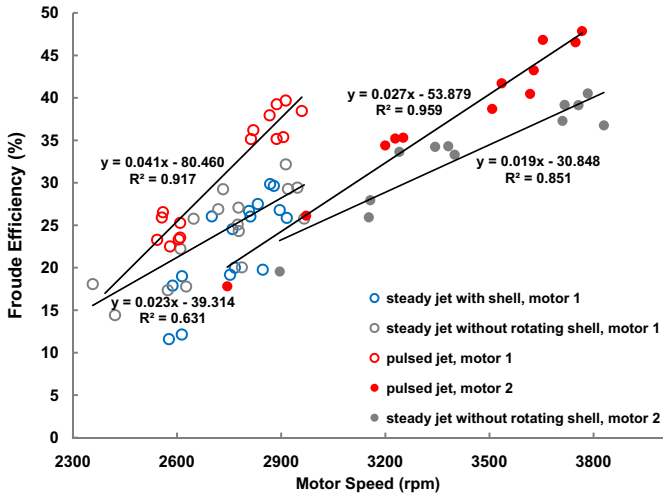

Figure 4.12. Compiled results for the measure of Froude efficiency versus motor speed.

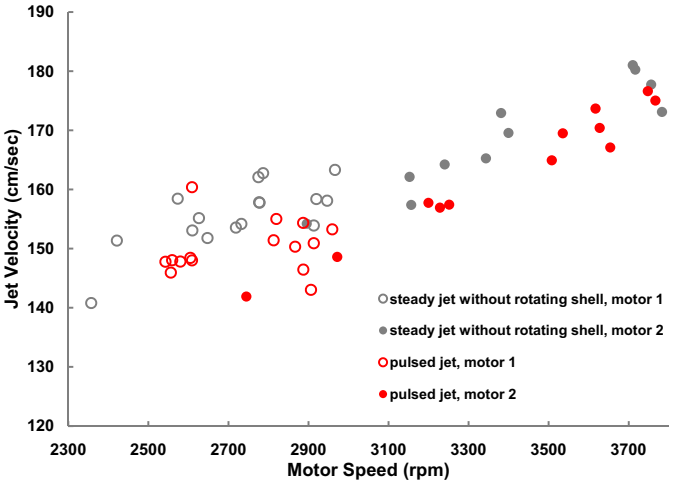

Figure 4.13. Graph of jet speed versus motor speed. An increase of motor speed is necessary with the second motor to produce an equivalent jet speed generated using the initial motor.

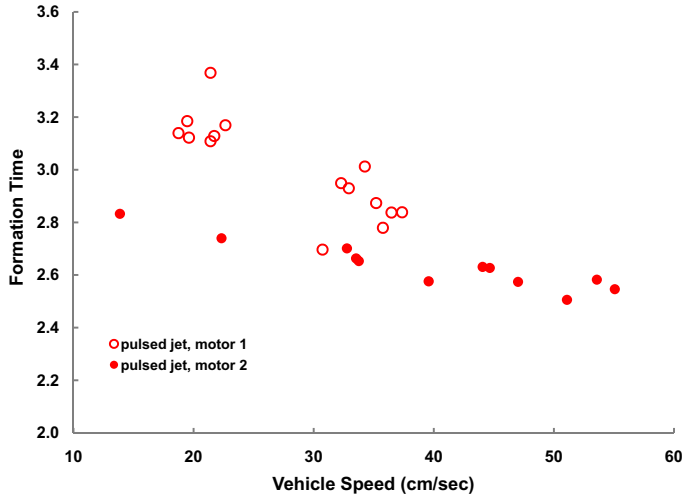

Figure 4.14. Formation time versus vehicle speed.

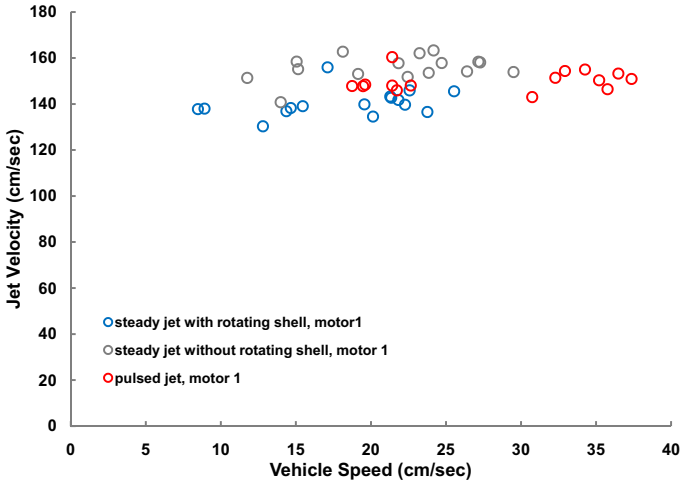

Figure 4.15. Graph of jet speed versus motor speed. Jet speed approaching a steady state value of 160 cm/s.

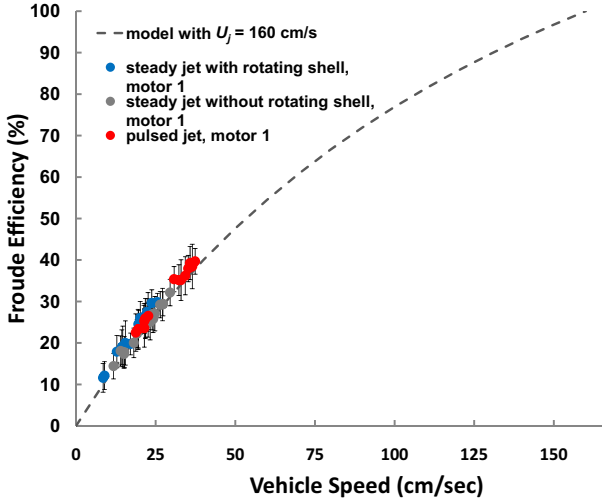

Figure 4.16. Graph of Froude efficiency versus vehicle speed. Possibility of further improvement at higher vehicle speeds.

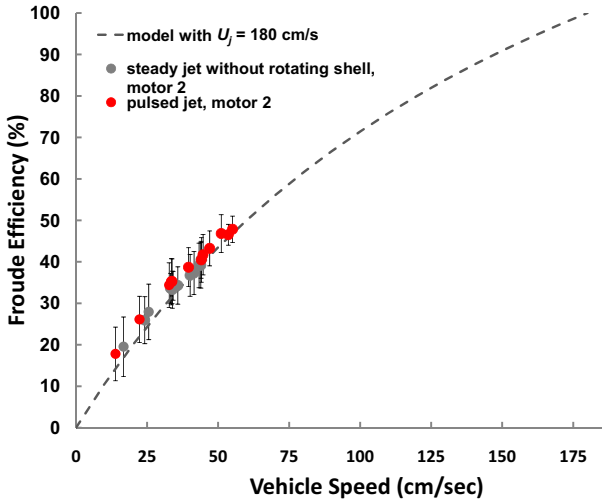

Figure 4.17. Graph of Froude efficiency versus vehicle speed. Demonstration of increased propulsive performance at higher vehicle speeds.

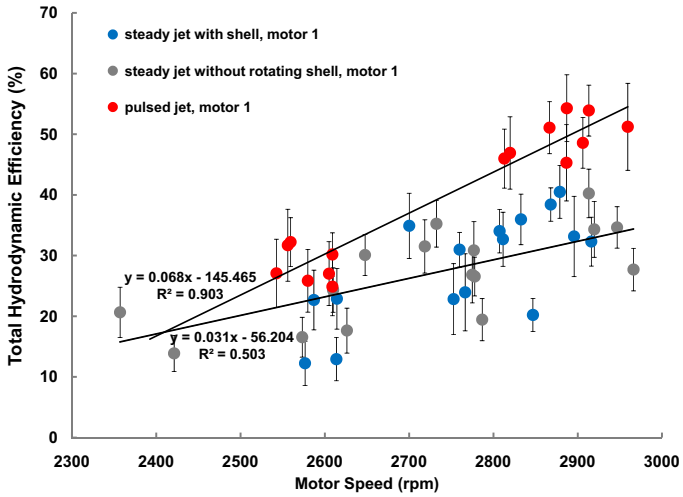

Figure 4.18. Total hydrodynamic efficiency versus motor speed for motor 1.

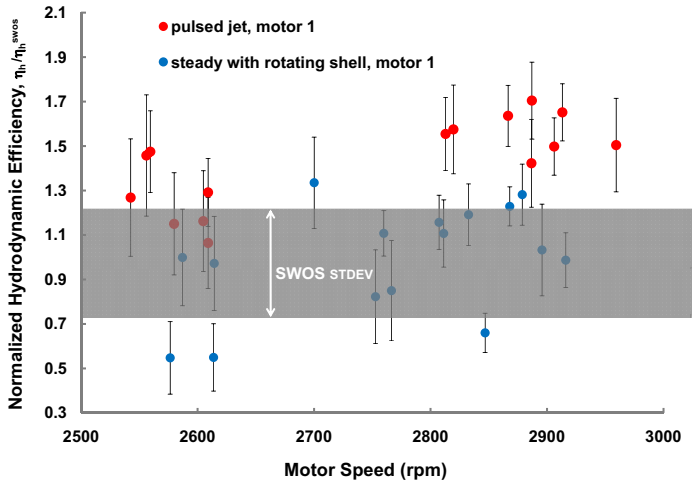

Figure 4.19. Normalized total hydrodynamic efficiency versus motor speed for motor 1.

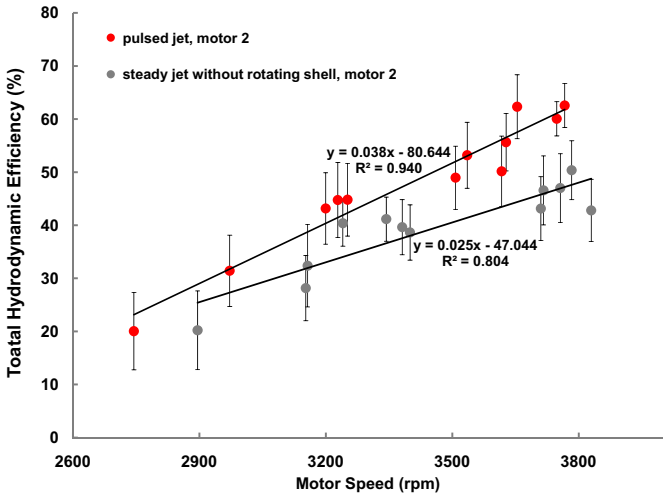

Figure 4.20. Total hydrodynamic efficiency versus motor speed for motor 2.

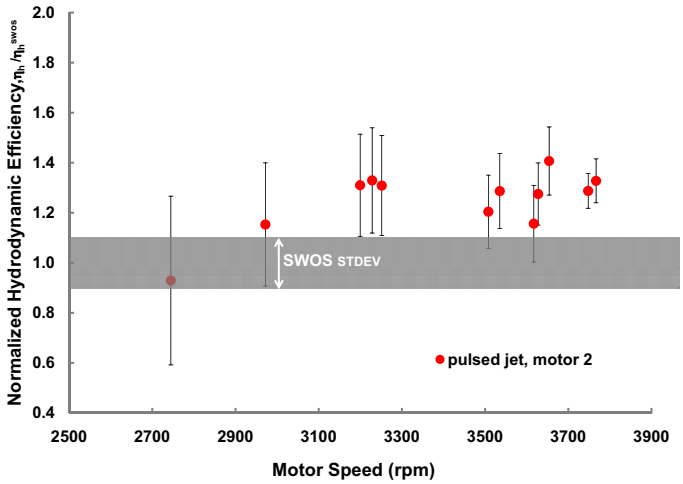

Figure 4.21. Normalized total hydrodynamic efficiency versus motor speed for motor 2.

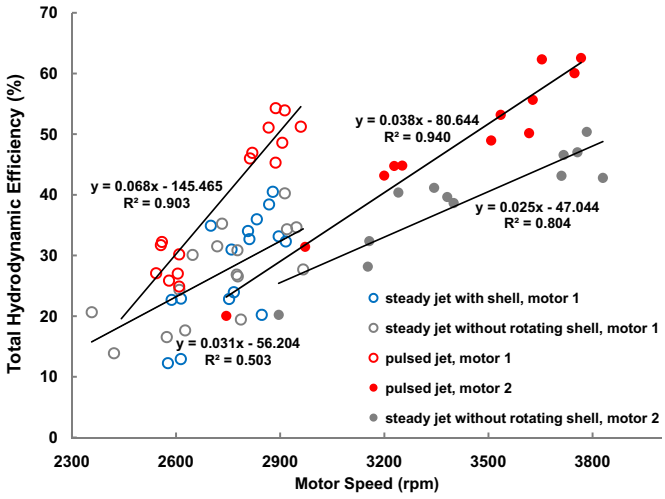

Figure 4.22. Compiled total hydrodynamic efficiency versus motor speed.

4.5 Comparison of Propulsive Efficiency to Other Biological Organisms

Biological organisms have been shown to display high propulsive efficiencies due to the production of vortex rings during propulsion. Squid have been shown to achieve propulsive efficiencies as high as 57.5% at a swimming speed of 9 cm/s, Bartol et al. (2001). At the highest swimming speed of 27 cm/s, the Froude efficiency decreased to 45%. Anderson and DeMont (2000) showed similar results for a 0.2 kg squid swimming at 50 cm/s. The measured average Froude efficiency reached 56%. Tytell and Lauder (2004) was able to measure the Froude efficiency of a steady swimming eel at 1.4 L s^{-1}, which was estimated to range from 50% to as high as 87%. Nauen and Lauder (2002) measured an average Froude efficiency of 74% for rainbow trout swimming at 1.2 Ls^{-1}. In comparison to the Froude efficiency achieved by biological organisms, as illustrated in figure 4.17, the highest measured Froude efficiency for the pulsed jet, propeller driven vehicle was 48% produced at a speed of 55 cm/s. This result in Froude efficiency is close to what has been measured of biological organisms. Furthermore, at higher vehicle speeds, the vehicle may achieve an increased Froude efficiency.

4.6 Comparison of Power Consumption for Both Steady and Unsteady Jet Propulsion

The pulsed jet configuration showed increased propulsive performance in comparison to the steady jet configuration both with and without the inner rotating shell. The power consumed by the motor, P_{input}, was measured to determine if a trade-off exists between improved propulsive performance and power consumption. Using power measurements, a power coefficient, (4.4), was defined similar to the approach utilized by Krueger (2006), Schultz and Webb (2002), Tytell (2004), and Tytell and Lauder (2004).

$$C_p = \frac{P_{input}}{\frac{1}{2}\,\rho\,S\,{U_v}^3}, \tag{4.4}$$

where ρ is the fluid density, S is the wetted surface area of the vehicle, and U_v is the averaged vehicle speed.

As the motor speed increases, the power coefficient significantly decreases for both modes of propulsion. See figure 4.23. The error bars denote the uncertainty in C_p, taking into account the error in the measurement of power. Data points where the error bars are not visible are a result of the error being smaller than the size of the data marker. At the lower motor speeds, a significant portion of the power supplied to the motor is used to overcome the static friction on the pillowblocks before the vehicle begins to move. This results in a higher C_p. At higher motor speeds, the ratio of power supplied to increase the velocity of the vehicle to the power supplied to overcome friction, is higher, resulting in a lower value for C_p. It is advantageous to minimize C_p. This can be accomplished by increasing the velocity of the vehicle while supplying less power. A trend line was used to fit a curve through the steady jet configuration data. The curve fit was used to normalize C_p by the baseline case of the steady jet without the rotating shell. See figure 4.24.

A normalized power coefficient value of 1 for all motor speeds denotes the baseline case for the steady jet without the rotating shell. The gray band represents the uncertainty in the measurement. The error bars indicate the uncertainty in the normalized power coefficient taking into account the error in the measurement of power. Although the pulsed jet configuration utilizes additional power to rotate the planetary gear system, the enhanced thrust production leads to an equivalent or smaller power coefficient in comparison to the steady jet configuration with the exception of two data points. The reduced cost in power for pulsed jet propulsion is most significant at the highest motor speeds. At the highest motor speed the normalized power coefficient is 37% less than the power coefficient for steady jet propulsion.

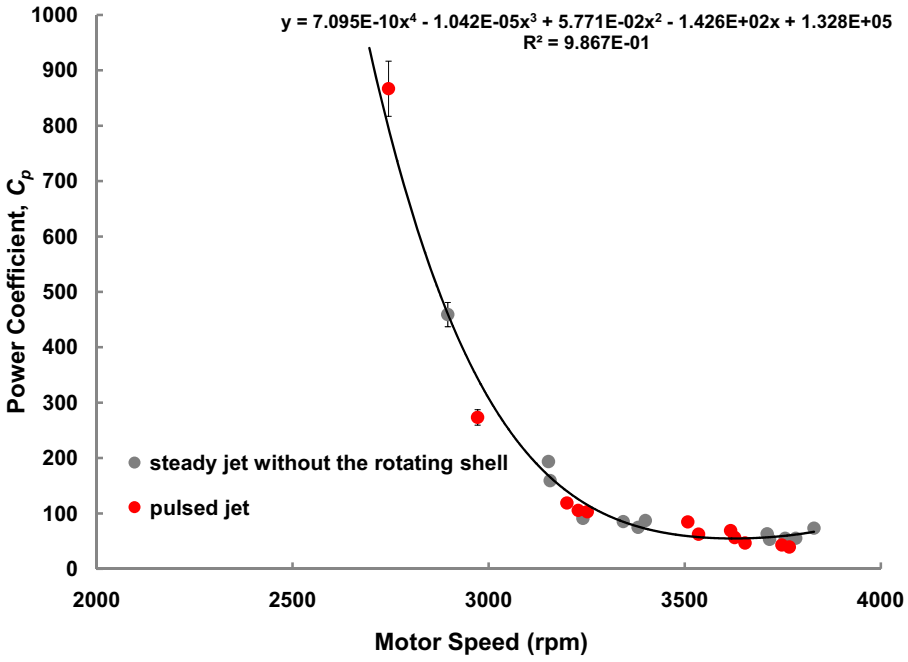

Figure 4.23. Graph of power coefficient versus motor speed illustrates increasing motor speed for both modes of propulsion results in a lower power coefficient.

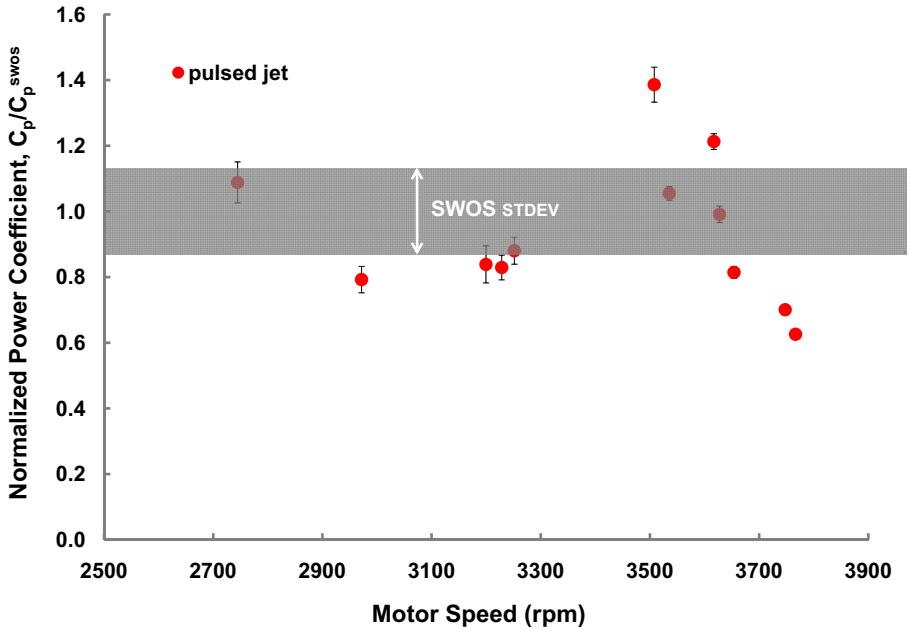

Figure 4.24. Graph of normalized power coefficient versus motor speed. Power coefficient of pulsed jet propulsion is equivalent or less than the steady jet power coefficient.

4.7 Conclusion

From the DPIV experiments, it was determined that an inner shell opening of 334^o was necessary to produce a pulsed jet with vortex ring formation for the studies with a Re_j equal to 5443 and a pulsing frequency of 2.5 Hz. This inner shell geometry was selected for the propulsive performance studies. From the PLIF experiments, it was evident that the wake of the pulsed jet was larger in size in comparison to the wake of the steady jet. This increase in wake size was attributed to the entrainment of the ambient fluid into the vortex during the vortex ring formation.

Two sets of propulsive performance studies were conducted using two distinct motors of the same model. The pulsed jet configuration had a 40% average increase in Froude efficiency at higher motor speeds when utilizing the initial motor. This increase dropped by 50% when the motor was replaced. This decrease in performance was shown to have resulted from the need to increase motor speed to obtain an equivalent jet speed as generated by the initial motor. This increase in motor speed led to a decrease in vortex ring formation time, and consequently, a decrease in the fluid impulse of the vortex. A model of the Froude efficiency versus vehicle speed was generated by supplying a value of 180 cm/s for U_{avg}, the expected maximum steady state jet velocity. Initial studies suggested that there may be further increases in the Froude efficiency at higher motor speeds. Due to mechanical failure of the initial motor used in the experiments, experiments were conducted at higher vehicle speeds using a second motor. With increased vehicle speed, the Froude efficiency reached a maximum value of 47% for the pulsed jet configuration. Information as to whether the Froude efficiency would continue to increase could not be determined from the data. Further higher speed experiments are necessary. It is important to note that as the body velocity approaches the jet velocity, the thrust approaches zero.

A second metric was used to measure the propulsive performance. The total hydrodynamic efficiency was measured for the two sets of experiments. The pulsed jet acquired a maximum total hydrodynamic efficiency of 54% at a motor speed of 2890 rpm with the initial motor. A further increase was measured for the total hydrodynamic efficiency for the second set of experiments, reaching a value 63% at a motor speed of 3770 rpm. Initial studies of motor speeds over 2800

rpm show a 57% increase in the total hydrodynamic efficiency of the pulsed jet in comparison to the steady jet. This increase in hydrodynamic efficiency dropped to 32% for the second set of experiments. The decrease in performance for the second motor can be attributed to a decrease in the vortex ring formation time.

The power consumed by the motor during propulsion was measured to determine if a trade-off exists between improved propulsive performance and power consumption. As the motor speed increased, the power coefficient significantly decreased for both modes of propulsion. Although the pulsed jet configuration utilizes additional power to rotate the planetary gear system, the enhanced thrust production leads typically to an equivalent or smaller power coefficient in comparison to the steady jet configuration without the rotating shell. The largest benefit with regard to reduced pulsed jet propulsion power cost is at the highest motor speeds. At these speeds, the normalized power coefficient was 37% less than the power coefficient for the steady jet propulsion configuration.